Research Article Vol. 15, No. 2 / 1 Feb 2025 / Optical Materials Express 299
Optical Materials EXPRESS

Fabrication of low-loss lithium niobate on insulator waveguides on the wafer scale [Invited]

MOHAMMADREZA YOUNESI,[1,*] THOMAS KÄSEBIER,[2] ILIA ELMANOV,[1] YANG-TENG LI,[1,3] PAWAN KUMAR,[1] REINHARD GEISS,[4] THOMAS SIEFKE,[2,4] FALK EILENBERGER,[2,4] FRANK SETZPFANDT,[1,4] UWE ZEITNER,[4,5] AND THOMAS PERTSCH[1,4]

[1]*Abbe Center of Photonics, Friedrich Schiller University, Albert-Einstein-Str. 6, 07745 Jena, Germany*
[2]*Institute of Applied Physics, Friedrich Schiller University, Albert-Einstein-Str. 15, 07745 Jena, Germany*
[3]*now at Genius Electronic Optical, Keya E Rd, Daya District, Taichung City 428, Taiwan*
[4]*Fraunhofer Institute for Applied Optics and Precision Engineering IOF, Albert-Einstein-Str. 7, 07745 Jena, Germany*
[5]*Department of Applied Sciences and Mechatronics, Hochschule München, Lothstr. 34, 80335 Munich, Germany*
[*]*mohammadreza.younesi@uni-jena.de*

Abstract: We report on the wafer scale fabrication of single-mode low-loss lithium niobate on insulator waveguides utilizing a chemically amplified resist and an optimized dry etching method. The fabricated single-mode waveguides are free of residuals and re-deposition, with measured losses for straight waveguides around 2 dB/m (0.02 dB/cm). We present a method offering advantages for large-scale production mainly due to its cost-effectiveness and faster writing time. This work holds promise for advancing integrated photonics and optical communication technologies.

1. Introduction

Lithium niobate on insulator (LNOI) is a widely-used substrate for different applications in nonlinear optics, electro-optics, and acousto-optics due to its versatile properties and large refractive index contrast, which makes it a promising platform for photonic integrated circuits (PICs) [1,2]. Such PICs are ideal candidates to enable the second quantum revolution by facilitating the control of quantum states on a large scale platform [3]. LNOI-based PICs have applications beyond quantum technologies, such as coherent communication systems and ultrafast signal processing [4–6]. For the continued development of LNOI PICs, a fabrication scheme is required to enable (i) low loss waveguides, ensuring their practicality and scalability in real-world applications, (ii) cost effectiveness, (iii) high flexibility in fabrication of different structures, and (iv) wafer scale operation.

Among various fabrication techniques, electron beam lithography (EBL) is a prevalent method for realization of PICs, where an electron beam defines the pattern of waveguides and other structures in a sensitive electron beam (e-beam) resist, followed by different pattern transfer processes to etch the LN layer. Achieving flexibility is feasible through high throughput character projection EBL (CP-EBL) which is a compatible method with the processes from Semiconductor Equipment and Materials International (SEMI). In this method, pre-defined cell structures are projected onto a substrate using an electron beam, enabling precise patterning at the nanoscale [7]. Furthermore, since writing speed is up to two orders of magnitude quicker than conventional Gaussian EBL, this provides a good balance between cost efficiency and flexibility.

#540146 https://doi.org/10.1364/OME.540146
Journal © 2025 Received 22 Aug 2024; revised 17 Oct 2024; accepted 21 Oct 2024; published 24 Jan 2025

Optical Materials EXPRESS

Waveguide losses stem from the intrinsic material absorption of lithium niobate (LN) and scattering from the waveguide. The scattering is increased by sidewall roughness of the waveguide. The sidewall roughness are the imperfection and irregularities in the shape of the waveguide, which leads to coupling between different guided modes of the waveguide and from the guided modes to radiation modes, increasing the propagation loss [8]. The sidewall roughness arises from the fabrication process, including imperfections in the shape of the mask used for the etching, anisotropy in the etching processes, and the material quality of LN. Controlling and reducing the sidewall roughness results in high-quality waveguides and low propagation loss.

Many different methods were previously reported for realizing high-quality and low loss waveguides in LNOI using EBL. The main methods with the lowest propagation losses which are widely used are chemo-mechanical polishing and dry etching. For the chemo-mechanical polishing technique, the desired structures are patterned as a chromium (Cr) mask on the surface of LN, and the pattern is transferred into LNOI using a wafer polishing machine. This method has been used for fabrication of low-loss structures with propagation loss of around 1 dB/m [9–14]. However this method is not compatible with standard fabrication processes and the fabricated waveguides have a large sidewall angle preventing high integration density.

Alternatively, nanostructuring of LN through utilization of a patterned mask on its surface, followed by transferring the pattern into LN using dry etching techniques shows promise for fabricating high-quality LNOI waveguides. Extensive research employing various etching methods and diverse mask materials has been conducted. Among the notable achievements, Zhang et al. demonstrated exceptional results by fabricating low-loss LNOI waveguides, achieving a propagation loss of 2.7 dB/m [15]. In this well-established fabrication method, the waveguides are fabricated using a thick hydrogen silsesquioxane (HSQ) resist layer, directly as the mask for etching into LN [10,16–18]. This resist can provide high resolution and thick mask with a good selectivity and it can be used for directly etching into LN. Although HSQ offers a very high resolution, the required dose and thus writing time for pattering the resist is prohibitive for wafer scale applications. These properties make HSQ disadvantageous for volume production.

Compared to HSQ, chemically amplified resist (CAR) needs smaller dose and writing time, since it contains a photochemical acid generator (PAG), which acts as catalyst in the exposure process to increase the sensitivity of the resist [19]. The primary drawback of many CARs is their limited selectivity, necessitating the use of an intermediate hard mask. Previously many different research groups have published their results in realization of low-loss structures using different masks such as silicon dioxide (SiO_2) and Cr [20–24]. The reported waveguides have loss in the range of 20 dB/m. Even though the measured losses are comparable to the best losses reported, the process can be improved, further reducing the waveguide losses. Here we enhance this process, reducing the waveguide losses comparable to those fabricated using the chemo-mechanical polishing technique.

In this paper, we propose a fabrication method relying on a CAR with a minimized e-beam exposure dose, an intermediate hard mask and a refined dry etching processes for realization of low loss waveguides without using HSQ resist. First, the fabrication route is demonstrated in detail and afterwards loss measurement results from racetrack resonators are presented. In the final part, we calculate the propagation loss of the straight waveguide using numerical calculations.

2. Fabrication

Utilizing CARs and an intermediate hard mask is a technology more suited to high-volume production [25] due to its lower exposure dose value and writing time. Among different CAR resists, we use FEP 171 with a dose value of 10 $\mu C/cm^2$, which is much smaller compared to the dose value needed for patterning HSQ resist (~5000 $\mu C/cm^2$).

Optical Materials EXPRESS

Our approach to fabricating low-loss waveguides involves the use of an intermediate Cr hard mask, as illustrated in Fig. 1. The substrate utilized in this study is X-cut LNOI supplied by NANOLN Co., which consists of a 600 nm thick LN layer atop a 2 μm layer of SiO_2, and a 525 μm thick silicon (Si) handling layer. The samples are prepared on 4-inch wafers. Initially, we deposit a 120 nm thick Cr layer onto the sample using ion beam deposition (Oxford Ionfab 300+ LC), followed by spin coating of a 300 nm thick FEP 171 resist layer (see Fig. 1(a)). This resist thickness is sufficient for etching through the 120 nm Cr layer to transfer the pattern into the hard mask.

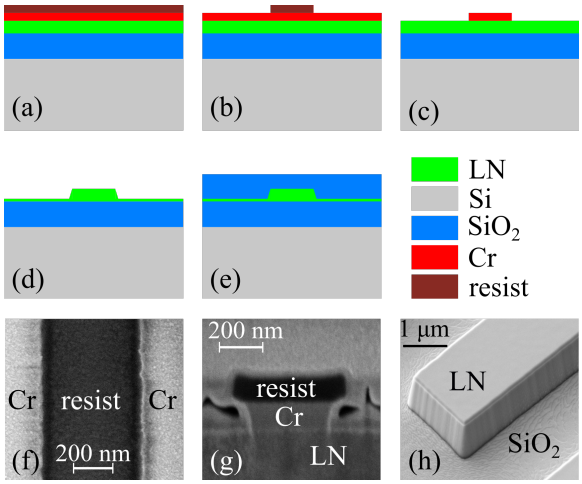

Fig. 1. Fabrication steps. (a) deposition of Cr layer and resist (b) patterning the resist (c) RIE etching of Cr layer (d) ICP-RIE etching of LN (e) annealing and cladding the structures with a layer of SiO_2. (f) Scanning electron microscopy image of the sample after the resist development. (g) Focused ion beam cross-section of the structures after the Cr etching step. (h) Scanning electron microscopy image of the sample after the final cleaning.

Next, the resist is exposed using a variable shaped beam (VSB) electron beam writer (Vistec SB350 OS) in multi-pass writing mode [7], which enhances dose uniformity and minimizes stitching errors, charging effects, and thermal loading. After exposure, the resist is developed (Fig. 1 (b) and (f)) to define the structures, and the pattern is transferred into the hard mask using reactive ion etching (Sentech SI-591) (Fig. 1 (c)). Figure 1 (g) presents a cross-sectional image of the etched Cr layer with the remaining resist layer on top, revealing an underetching of approximately 100 nm that should be considered during sample design. Finally, etching into the LN layer (Fig. 1 (d)) is performed using inductively coupled plasma reactive ion etching (ICP-RIE) with CHF_3 gas.

One of the main challenges we faced in nanostructuring LNOI is the formation of an amorphous layer caused by the re-deposition of material removed from the LNOI substrate during the etching process, which adheres to the fabricated nanostructures [26]. Although methods like chemical cleaning or ion milling [27,28] have been introduced to remove these re-deposition layers, they can inadvertently increase sidewall roughness on the waveguides. The most effective way to address this issue is to optimize the fabrication process itself to prevent the amorphous layer from forming in the first place. Previous studies have shown that in ICP-RIE etching, optimizing parameters such as chamber pressure and DC bias can control the re-deposition layer [26]. In our fabrication development, we refined the etching conditions for patterning LN to ensure the production of high-quality structures without any visible re-deposition. Since etching LN involves fluorine chemistry, there is a high likelihood of generating by-products like LiF, which

Optical Materials EXPRESS

can negatively impact the quality of the final structures. Our experiments demonstrate that by lowering the substrate electrode temperature during the ICP-RIE process, no residuals are observed on the surfaces of the structures. Reducing the temperature alters the reaction kinetics of the process, preventing residuals from being absorbed onto the LN surface and allowing them to be pumped out of the chamber.

Subsequently, we cleaned the sample and prepared it for measurement. To remove the residuals of the Cr layer, we employed a commercial etching mixture composed of ceric ammonium nitrate and perchloric acid. An additional cleaning step involved using an etching mixture of phosphoric acid, nitric acid, and acetic acid in a megasonic bath at 50°C for one hour. This process effectively removes the passivation layer from the surface of the structures and results in very smooth sidewalls. Figure 1 (h) displays a fabricated structure after the etching and cleaning processes, demonstrating that no residuals or re-depositions are visible on the sidewalls of the waveguides. We then annealed the sample in an oxygen (O_2) atmosphere at ambient pressure, maintaining a temperature of 520°C for two hours. This procedure reduces the loss in the waveguides by enhancing the crystallinity of the LN [10,16]. Finally, we applied a SiO_2 cladding layer to the sample using plasma-enhanced chemical vapor deposition to enhance the mode field distribution and provide additional protection (see Fig. 1 (e)).

3. Discussion and results

To measure the propagation losses of the fabricated structures, we fabricated racetrack resonators. The schematic of our structure is illustrated in Fig. 2 (a). Light is coupled into the waveguide using the edge coupling method, and this light is then evanescently coupled into the racetrack resonator within the gap region. The transmitted light is collected with a lensed fiber, detected with a photodetector, and used for calculation of the waveguide loss in the resonator. In our structures, the LN layer is etched for 500 nm, the top width of the structures for the waveguide and racetrack resonators is 1 μm. We fabricated and tested four racetrack resonators with straight waveguide lengths (L_s) of 100 μm, 300 μm, 400 μm, and 500 μm. Each resonator features a bend radius of 100 μm, and the gap between the waveguide and the resonator in the coupling region is 300 nm. An scanning electron microscopy image of a waveguide and resonator manufactured with these parameters is presented in Fig. 2 (b).

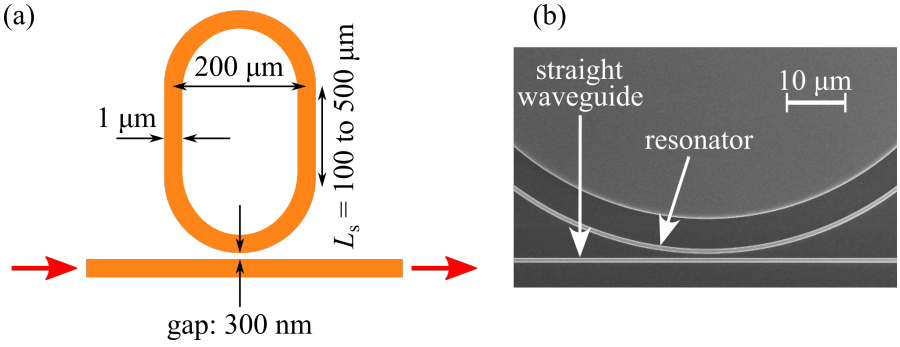

Fig. 2. (a) Schematic of the racetrack resonator and waveguide. (b) Scanning electron microscopy image of a fabricated straight waveguide and a resonator.

The total loss of the resonator stems from two effects: the scattering and absorption loss in the ring resonator (propagation loss) and the loss due to the coupling to the waveguide (coupling loss). To estimate the loss values, we performed transmission measurements of the racetrack resonator. For the resonator with L_s of 400 μm, the detected signal for the TE mode in the wavelength range of 1547 to 1553 nm is shown in Fig. 3 (a). In the next step, the resonances

Optical Materials EXPRESS

in the spectrum are fitted using a Lorentzian function and normalized to the transmitted power outside of resonances. One of the resonances at the wavelength of 1548.818 nm and its fit is shown in Fig. 3 (b). From the fitted data for the resonances, we calculated the value of the loaded quality factor (Q) and the group index (n_g) of each resonance as

$$Q = \frac{\lambda_0}{\Delta\lambda} \tag{1}$$

and

$$n_g = \frac{\lambda_0^2}{F \times L_{tot}}, \tag{2}$$

where λ_0 and $\Delta\lambda$ are the central wavelength and full width at half maximum of each resonance (Fig. 3 (b)), and F and L_{tot} are free spectral range of the resonances and total length of the resonator respectively. These values allow us to calculate two loss coefficients $\alpha_{1,2}$ and the corresponding loss values $l_{1,2}$ as

$$\alpha_{1,2} = \frac{\pi n_g}{Q\lambda}(1 \pm \sqrt{T}) \tag{3}$$

and

$$l_{1,2} = -10\log\left(e^{-\alpha_{1,2}\times 1[m]}\right), \tag{4}$$

where T is the minimal transmission of the normalized fit (Fig. 3 (b)) [29,30]. One of the calculated loss values relates to the propagation loss and the other one to the coupling loss of the racetrack resonator. If these two values are equal, the propagation and coupling loss values are the same and the resonator works in the critical coupling regime, which is not always the case.

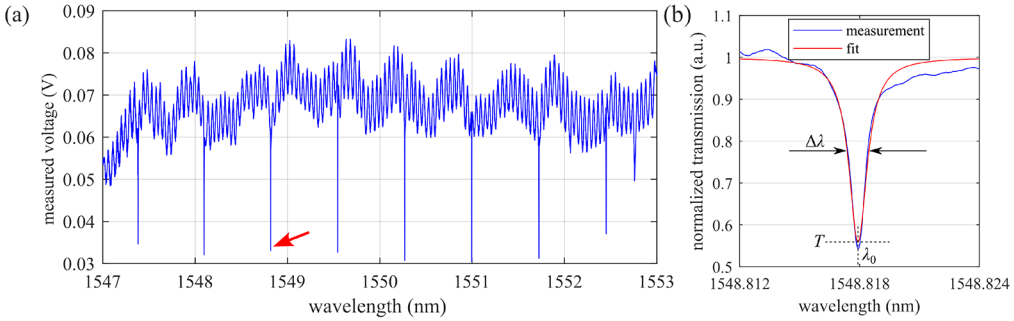

Fig. 3. (a) Measured voltage corresponding to the transmitted signal of the resonator, in the range of 1547 to 1553 nm. (b) The resonance at 1548.818 nm (marked as red arrow in (a)) and the Lorentzian fit function. The plots are normalized to 1.

For the resonator with a L_s of 400 μm, and within the measured wavelength range shown in Fig. 3 (a), the average Q is $(0.83 \pm 0.15) \times 10^6$ and n_g is 2.32 ± 0.02. The corresponding loss values are $l_1 = 7.8 \pm 2.2$ dB/m and $l_2 = 43.7 \pm 8.9$ dB/m. These results indicate that our resonator is not operating in the critical coupling regime. Similar measurements and calculations were performed for the other three fabricated resonators, and the values for the Q-factor, l_1, and l_2 for all four resonators are presented in Table 1. The table demonstrates that the calculated loss values are consistent across all resonators, indicating good repeatability in our experiments.

The best-performing resonator is the one with L_s of 500 μm, where the measured l_1 is 4.9 ± 1.4 dB/m and l_2 is 26.6 ± 5.3 dB/m. To determine which of the two measured losses corresponds to the actual propagation loss of the waveguide and which represents the coupling loss, we conducted simulations using the dimensions of the measured racetrack resonator. The coupling loss determined from the simulation is 28.97 dB/m which is close to the measured loss l_2. It is

Optical Materials EXPRESS

Table 1. The extracted parameters from the measured racetrack resonators with different straight waveguide length (L_s).

L_s [μm]	average Q	l_1 [dB/m]	l_2 [dB/m]
100	$(1.29 \pm 0.34) \times 10^6$	7.8 ± 3.9	26.5 ± 8.9
300	$(0.95 \pm 0.11) \times 10^6$	6.2 ± 2.7	37.0 ± 6.4
400	$(0.83 \pm 0.15) \times 10^6$	7.8 ± 2.2	43.7 ± 8.9
500	$(1.34 \pm 0.24) \times 10^6$	4.9 ± 1.4	26.6 ± 5.3

safe to assume that l_1 is the propagation loss of the waveguide, while l_2 represents the coupling loss. In other words, our resonator is working in the strong coupling regime and the propagation loss (l_p) and coupling loss (l_c) values in the wavelength range of 1447 to 1553 nm for TE mode are around 5 dB/m and 27 dB/m respectively. We also performed similar measurements and analysis for the TM mode of the resonator and the measured propagation loss for the same wavelength range for TM mode is around 8 dB/m. The propagation loss has two different contributions: straight waveguide loss and bend loss. We expect the propagation loss for the straight waveguide to be smaller than the measured value for the entire racetrack resonator, hence we carried out the following calculations to find the actual loss of the straight waveguide.

The calculated propagation loss values explained previously are under the assumption of having identical propagation loss for straight and curved parts of the racetrack resonator. This assumption is generally not true because the losses induced by waveguide bending are not considered. Here, we separate these two losses and calculate the propagation loss of the straight waveguide.

Since the measured resonator is working in the strong coupling regime, the propagation (α_p) and coupling (α_c) loss coefficients can be calculated from Eq. (3) as

$$\alpha_p = \frac{\pi n_g}{Q\lambda}(1 - \sqrt{T}) \tag{5}$$

and

$$\alpha_c = \frac{\pi n_g}{Q\lambda}(1 + \sqrt{T}). \tag{6}$$

Under the assumption of small losses and small coupling one can get equations to calculate coupling and propagation losses, constructing a system of two equations [29]:

$$\frac{1}{Q} = \frac{\alpha_p \lambda}{2\pi n_g} + \frac{\alpha_c \lambda}{2\pi n_g} \tag{7}$$

$$\frac{\alpha_c}{\alpha_p} = \frac{1 + \sqrt{T}}{1 - \sqrt{T}}, \tag{8}$$

where λ is the central wavelength of the measured bandwidth (here it is 1550 nm). Separating the loss coefficients for the straight (α_s) and curved (α_r) parts of the resonator with $\alpha_p = \alpha_s + \alpha_r$, the equations change as

$$\frac{1}{Q} = (\alpha_r + \alpha_s + \alpha_c)\frac{\lambda}{2\pi n_g} \tag{9}$$

and

$$\frac{\alpha_c L_{tot}}{\alpha_r 2\pi R + \alpha_s 2L_s} = \frac{1 + \sqrt{T}}{1 - \sqrt{T}}, \tag{10}$$

where R is the bending radius and L_s is the length of straight parts of the resonator (as it is shown in Fig. 2 (a)). These two equations contain three unknown values and solving it requires an

Optical Materials EXPRESS

additional equation. To solve this problem, we compare the measurement results for two similar racetrack resonators which are only different in the length of straight waveguide L_s. We carried out measurements for two resonators with L_s of 100 and 500 μm in the range of 1447 to 1553 nm. Since these two resonators have only different L_s compared to previously measured resonator, we assume that both resonators are working in the strong coupling regime and they have equal α_r and α_s and different α_c. This adds two more equations and one more unknown variable. Labeling the corresponding parameters for resonators with L_s of 100 and 500 μm respectively by I and II, the system of equations is now

$$\begin{pmatrix} (1-\sqrt{T^{\mathrm{I}}})L_{\mathrm{tot}}^{\mathrm{I}} & -(1+\sqrt{T^{\mathrm{I}}})2\pi R & -(1+\sqrt{T^{\mathrm{I}}})2L_s^{\mathrm{I}} & 0 \\ 1 & 1 & 1 & 0 \\ 0 & -(1+\sqrt{T^{\mathrm{II}}})2\pi R & -(1+\sqrt{T^{\mathrm{II}}})2L_s^{\mathrm{II}} & (1-\sqrt{T^{\mathrm{II}}})L_{\mathrm{tot}}^{\mathrm{II}} \\ 0 & 1 & 1 & 1 \end{pmatrix} \begin{pmatrix} \alpha_c^{\mathrm{I}} \\ \alpha_r \\ \alpha_s \\ \alpha_c^{\mathrm{II}} \end{pmatrix} = \begin{pmatrix} 0 \\ \frac{2\pi n_g}{Q^{\mathrm{I}}\lambda} \\ 0 \\ \frac{2\pi n_g}{Q^{\mathrm{II}}\lambda} \end{pmatrix}. \quad (11)$$

Solving the equations, we calculate interval values for α_c^{I}, α_c^{II}, α_r, and α_s with 90% confidence intervals and then using an exponential equation similar to Eq. (4) we calculate the corresponding loss values $l_c^{\mathrm{I}} = 24.23 \pm 7.70$ dB/m, $l_c^{\mathrm{II}} = 22.02 \pm 4.83$ dB/m, $l_r = 11.37 \pm 3.37$ dB/m, and $l_s = 0.37 \pm 1.74$ dB/m. This shows that the propagation loss for TE mode in the straight waveguide is highly likely less than 2 dB/m, with good potential to be well below 1 dB/m.

4. Conclusion and outlook

In this work, the fabrication of LNOI waveguides using dry etching is investigated. With the focus on smooth sidewalls for low loss, a suitable process based on the ICP-RIE dry etching method is found. We used FEP 171 which has a small dose value compared to other resists and is a good candidate for volume production. We optimized the fabrication process to avoid the residuals and re-deposition layer and achieved high-quality structures. Our measured overall propagation loss for the fabricated racetrack resonators for the TE mode is around 5 dB/m and for the TM mode is around 8 dB/m, which is in the range of the best loss reported in the literature. Further analysis shows that the propagation loss of straight waveguide section of the resonator is smaller and in the range of 2 dB/m.

Funding. Carl-Zeiss-Stiftung; Thüringer Ministerium für Wirtschaft, Wissenschaft und Digitale Gesellschaft (2021 FGI 0043 (Quantum Hub Thuringia)); Deutsche Forschungsgemeinschaft (PE 1524/13-1 (NanoPair), 398816777-SFB 1,375 (NOA)); Bundesministerium für Bildung und Forschung (13N14877 (QuantIm4Life), 13N16108 (PhoQuant)).

Acknowledgement. The sample fabrication within this work was carried out by the microstructure technology team at IAP Jena. The authors would like to thank them for providing the fabrication facilities, carrying out processes and providing support.

We acknowledge support by the German Research Foundation Projekt-Nr. 512648189 and the Open Access Publication Fund of the Thueringer Universitaets- und Landesbibliothek Jena.

Disclosures. The authors declare no conflicts of interest.

Data availability. Data underlying the results presented in this paper are not publicly available at this time but may be obtained from the authors upon reasonable request.

References

1. A. Boes, B. Corcoran, L. Chang, *et al.*, "Status and potential of lithium niobate on insulator (LNOI) for photonic integrated circuits," Laser Photonics Rev. **12**(4), 1700256 (2018).
2. G. Chen, N. Li, J. D. Ng, *et al.*, "Advances in lithium niobate photonics: development status and perspectives," Adv. Photonics **4**(03), 034003 (2022).
3. L. Lu, X. Zheng, Y. Lu, *et al.*, "Advances in chip-scale quantum photonic technologies," Adv. Quantum Technol. **4**(12), 2100068 (2021).
4. M. Xu, M. He, H. Zhang, *et al.*, "High-performance coherent optical modulators based on thin-film lithium niobate platform," Nat. Commun. **11**, 1 (2020).

Optical Materials EXPRESS

5. C. Wang, M. Zhang, X. Chen, *et al.*, "Integrated lithium niobate electro-optic modulators operating at CMOS-compatible voltages," Nature **562**(7725), 101–104 (2018).
6. H. Feng, T. Ge, X. Guo, *et al.*, "Integrated lithium niobate microwave photonic processing engine," Nature **627**(8002), 80–87 (2024).
7. M. Hädrich, T. Siefke, M. Banasch, *et al.*, "Optical metasurfaces made by cell projection lithography," Photonics Views **19**(5), 28–31 (2022).
8. C. G. Poulton, C. Koos, M. Fujii, *et al.*, "Radiation modes and roughness loss in high index-contrast waveguides," IEEE J. Sel. Top. Quantum Electron. **12**(6), 1306–1321 (2006).
9. C. Li, J. Guan, J. Lin, *et al.*, "Ultra-high Q lithium niobate microring monolithically fabricated by photolithography assisted chemo-mechanical etching," Opt. Lett. **31**, 31556–31562 (2023).
10. Q. Luo, C. Yang, R. Zhang, *et al.*, "On-chip erbium-doped lithium niobate microring lasers," Opt. Lett. **46**(13), 3275–3278 (2021).
11. R. Wu, J. Zhang, N. Yao, *et al.*, "Lithium niobate micro-disk resonators of quality factors above 10^7," Opt. Lett. **43**(17), 4116–4119 (2018).
12. R. Gao, B. Fu, N. Yao, *et al.*, "Electro-optically tunable low phase-noise microwave synthesizer in an active lithium niobate microdisk," Laser Photonics Rev. **17**(5), 2200903 (2023).
13. J. Lin, S. Farajollahi, Z. Fang, *et al.*, "Electro-optic tuning of a single-frequency ultranarrow linewidth microdisk laser," Adv. Photonics **4**(03), 036001 (2022).
14. M. Wang, R. Wu, J. Lin, *et al.*, "Chemo-mechanical polish lithography: a pathway to low loss large-scale photonic integration on lithium niobate on insulator," Quantum Engineering **1**(1), e9–10 (2019).
15. M. Zhang, C. Wang, R. Cheng, *et al.*, "Monolithic ultra-high-Q lithium niobate microring resonator," Optica **4**(12), 1536–1537 (2017).
16. A. Shams-Ansari, G. Huang, L. He, *et al.*, "Reduced material loss in thin-film lithium niobate waveguides," APL Photonics **7**(8), 081301 (2022).
17. T. Li, K. Wu, M. Cai, *et al.*, "A single-frequency single-resonator laser on erbium-doped lithium niobate on insulator," APL Photonics **6**(10), 101301 (2021).
18. Q. Luo, C. Yang, Z. Hao, *et al.*, "Integrated ytterbium-doped lithium niobate microring lasers," Opt. Lett. **47**(6), 1427–1430 (2022).
19. H. Ito, "Chemical amplification resists for microlithography," in *Advances in Polymer Science*, vol. 172 (Springer, 2005), pp. 37–245.
20. I. Krasnokutska, J.-L. J. Tambasco, X. Li, *et al.*, "Ultra-low loss photonic circuits in lithium niobate on insulator," Opt. Express **26**(2), 897–904 (2018).
21. K. Luke, P. Kharel, C. Reimer, *et al.*, "Wafer-scale low-loss lithium niobate photonic integrated circuits," Opt. Express **28**(17), 24452–24458 (2020).
22. M. Bahadori, Y. Yang, L. L. Goddard, *et al.*, "High performance fully etched isotropic microring resonators in thin-film lithium niobate on insulator platform," Opt. Express **27**(15), 22025–22039 (2019).
23. X. P. Li, K. X. Chen, and Z. F. Hu, "Low-loss bent channel waveguides in lithium niobate thin film by proton exchange and dry etching," Opt. Mater. Express **8**(5), 1322–1327 (2018).
24. Y.-X. Lin, M. Younesi, H.-P. Chung, *et al.*, "Ultra-compact, broadband adiabatic passage optical couplers in thin-film lithium niobate on insulator waveguides," Opt. Express **29**(17), 27362–27372 (2021).
25. R. Ikeno, S. Maruyama, Y. Mita, *et al.*, "Electron-beam lithography with character projection technique for high-throughput exposure with line-edge quality control," J. Micro/Nanolithogr., MEMS, MOEMS **15**(3), 031606 (2016).
26. F. Kaufmann, G. Finco, A. Maeder, *et al.*, "Redeposition-free inductively-coupled plasma etching of lithium niobate for integrated photonics," Nanophotonics **12**(8), 1601–1611 (2023).
27. G. Ulliac, V. Calero, A. Ndao, *et al.*, "Argon plasma inductively coupled plasma reactive ion etching study for smooth sidewall thin film lithium niobate waveguide application," Opt. Mater. **53**, 1–5 (2016).
28. M. R. Escalé, "Generation, modulation and detection of light in lithium niobate nanophotonic devices," Ph.D. thesis, ETH Zürich (2019).
29. R. Adar, Y. Shani, C. H. Henry, *et al.*, "Measurement of very low-loss silica on silicon waveguides with a ring resonator," Appl. Phys. Lett. **58**(5), 444–445 (1991).
30. P. An, V. Kovalyuk, A. Golikov, *et al.*, "Experimental optimisation of O-ring resonator Q-factor for onchip spontaneous four wave mixing," J. Phys.: Conf. Ser. **1124**, 051047 (2018).